GA–A24135

OVERVIEW OF RECENT EXPERIMENTAL RESULTS FROM THE DIII–D ADVANCED TOKAMAK PROGRAM

by
K.H. BURRELL for the DIII–D TEAM

NOVEMBER 2002

DISCLAIMER

GA–A24135

OVERVIEW OF RECENT EXPERIMENTAL RESULTS FROM THE DIII–D ADVANCED TOKAMAK PROGRAM

by
K.H. BURRELL for the DIII–D TEAM

This is a preprint of a paper to be submitted for publication in *Nucl. Fusion.*

Work supported by
the U.S. Department of Energy under
Contract No. DE-AC03-99ER54463

GENERAL ATOMICS PROJECT 30033
NOVEMBER 2002

ABSTRACT

The DIII-D research program is developing the scientific basis for advanced tokamak (AT) modes of operation in order to enhance the attractiveness of the tokamak as an energy producing system. Since the last International Atomic Energy Agency (IAEA) meeting, we have made significant progress in developing the building blocks needed for AT operation: 1) We have doubled the magnetohydrodynamic (MHD) stable tokamak operating space through rotational stabilization of the resistive wall mode; 2) Using this rotational stabilization, we have achieved $\beta_N H_{89} \geq 10$ for 4 τ_E limited by the neoclassical tearing mode; 3) Using real-time feedback of the electron cyclotron current drive (ECCD) location, we have stabilized the (m,n) = (3,2) neoclassical tearing mode and then increased β_T by 60%; 4) We have produced ECCD stabilization of the (2,1) neoclassical tearing mode in initial experiments; 5) We have made the first integrated AT demonstration discharges with current profile control using ECCD; 6) ECCD and electron cyclotron heating (ECH) have been used to control the pressure profile in high performance plasmas; and 7) We have demonstrated stationary tokamak operation for 6.5 s (36 τ_E) at the same fusion gain parameter of $\beta_N H_{89}/q_{95}^2 \cong 0.4$ as ITER but at much higher $q_{95} = 4.2$. We have developed general improvements applicable to conventional and advanced tokamak operating modes: 1) We have an existence proof of a mode of tokamak operation, quiescent H-mode, which has no pulsed, ELM heat load to the divertor and which can run for long periods of time (3.8 s or 25 τ_E) with constant density and constant radiated power; 2) We have demonstrated real-time disruption detection and mitigation for vertical disruption events using high pressure gas jet injection of noble gases; 3) We have found that the heat and particle fluxes to the inner strike points of balanced, double-null divertors are much smaller than to the outer strike points. We have made detailed investigations of the edge pedestal and SOL: 1) Atomic physics and plasma physics both play significant roles in setting the width of the edge density barrier in H-mode; 2) ELM heat flux conducted to the divertor decreases as density increases; 3) Intermittent, bursty transport contributes to cross field particle transport in the scrape-off layer (SOL) of H-mode and, especially, L-mode plasmas.

1. INTRODUCTION

The DIII–D research program is developing the scientific basis for advanced modes of operation in order to enhance the attractiveness of the tokamak as an energy producing system. Previous studies [1–6] have shown that an attractive tokamak requires high power density (which demands high toroidal beta $\beta_T = 2\ \mu_o \langle p \rangle / B_T^2$), high ignition margin (high energy confinement time τ_E), and steady-state operation with low recirculating power (high bootstrap fraction f_{BS}), as well as adequate divertor heat removal, particle and impurity control. These requirements demand an integrated approach, optimizing the plasma from the core, through the edge pedestal and into the divertor. To utilize advanced tokamak physics in future devices, we are developing predictive understanding validated in integrated physics demonstrations.

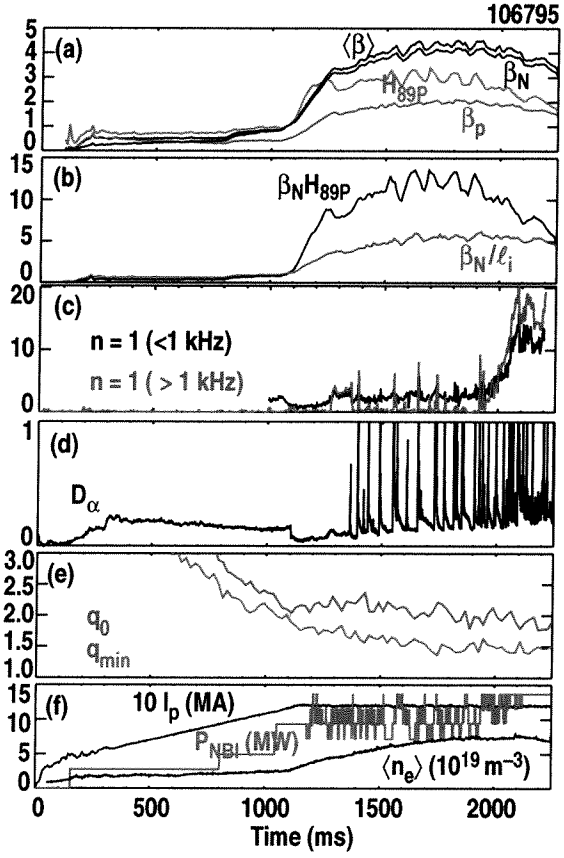

Fig. 1. Time history of high performance advanced tokamak shot 106795 with $\beta_N H_{89} \geq 10$ for 4 τ_E. (a) From top to bottom traces within this box: β_T, β_N, H_{89} and β_P. (b) $\beta_N H_{89}$ (top trace in box) and β_N/ℓ_i, where ℓ_i is the plasma internal inductance. (c) n=1 Mirnov amplitude for frequencies above and below 1 kHz; the <1 kHz traces up to 1900 ms show the presence of a small RWM, stabilized by rotation while the growth in both traces after 1900 ms is due to an NTM. (d) Divertor D_α trace. (e) $q(0)$ (upper trace) and minimum q_{min} (lower trace). (f) 10 x plasma current, neutral beam injected power and line averaged density.

Since the last International Atomic Energy Agency (IAEA) meeting, we have made substantial progress in creating the building blocks required for advanced tokamak (AT) plasmas. Techniques to increase the tokamak beta limits are part of these building blocks. By using rotational stabilization of the resistive wall mode (RWM), we have increased the β_T operating region stable to the external kink mode by about a factor of two up to the ideal wall beta limit [7–9]. As is shown in Fig. 1, we have utilized these techniques to produce AT discharges with $q_{min} \geqq 1.5$ and $\beta_N H_{89} \geqq 10$ which were sustained at that $\beta_N H_{89}$ level for 680 ms or about 4 τ_E [10]. Here, $\beta_N = (aB_T/I_p)\beta_T$ and H_{89} is the ratio of τ_E to the energy confinement time given by the

ITER89P scaling law [11]; a is the plasma minor radius (half width), B_T is the toroidal field and I_p is the plasma current. In terms of absolute parameters, these plasmas simultaneously achieve $\beta_T = 4.2\%$, fusion gain $\beta_T \tau_E = 0.66\%$ s, poloidal beta $\beta_p \cong 2$, bootstrap current fraction $f_{BS} \cong 0.65$ and total non-inductive current fraction $f_{NI} \cong 0.85$. The duration of the high performance phase in these discharges is limited by neoclassical tearingmodes (NTM) which become more unstable as the current profile evolves and the minimum safety factor q_{min} drops. This gives extra motivation to our NTM and current drive research.

We have demonstrated real time feedback stabilization of neoclassical tearing modes using electron cyclotron current drive (ECCD) for both the (m,n) = (3,2) [12,13] and, in preliminary experiments, the (m,n) = (2,1) mode [13,14]. The feedback system was used to precisely position the ECCD on the island in order to suppress the modes either by altering the toroidal field slightly (about 0.5%) or by small radial shifts of the plasma position [about 1 cm for the (3,2)]. In cases of (3,2) stabilization, β_T was increased 60% above the level in the presence of the mode, up to a level 20% above that achieved prior to the onset of the NTM. This latter stabilization was done in sawtoothing discharges, a reactor relevant regime. This real time feedback control represents the first use of active feedback control to position the ECCD and suppress the NTM.

Another part of the AT building block set is control of the profiles of current density and plasma pressure. Initial experiments integrating ECCD current profile control into high performance AT discharges were done with 2.5 MW of electron cyclotron (EC) waves in discharges with $q_{min} \gtrsim 2$, and $\beta_N{*}H_{89} = 7$ which were sustained for the 2 s length of the ECCD pulse or about 18 τ_E [15]. The total noninductive current driven in these shots reaches 90%. The q-profile changes associated with the ECCD trigger core barrier formation in these discharges, since both electron and ion thermal transport are reduced in the core of these discharges after the EC power is applied. ECCD has also been used to alter the current density profile in quiescent double barrier (QDB) plasmas [16].

Both electron cyclotron heating (ECH) and ECCD have been found to decrease peakedness of the plasma density profile in QDB discharges [16]. Applying EC power to an already formed core barrier results in some increase in core thermal transport but a much bigger increase in particle transport. The net result is that the density profile flattens much more than the pressure profile. Owing to the strong cryopumping of QDB discharges, density profiles in these plasmas are more peaked than desired, leading to significant impurity peaking [17]. This peaking is substantially reduced with EC from a ratio of 2.13, peak to line-averaged, to 1.5.

Utilizing some of the plasma control tools developed for the AT work, we have also demonstrated an improved operating scenario for ITER [18]. These discharges have the same

fusion power gain parameter $\beta_N H_{89}/q_{95}^2 \cong 0.4$ as ITER but at $q_{95} = 4.2$, significantly higher than the $q_{95} = 3$ in the ITER design.

In addition to the advanced tokamak research, a second theme in the DIII-D research over the past two years is the development of general tokamak improvements which are applicable to both the AT and conventional tokamak. Our work on the quiescent H-mode (QH-mode) demonstrates a solution to the pulsed divertor heat load in future burning plasma devices caused by edge localized modes (ELM) [17,19,20]. In addition, we have demonstrated disruption mitigation using a massive gas puff of either neon or argon [21-23]. This substantially reduces thermal and mechanical vessel loading while simultaneously suppressing runaway electrons in the current quench. For vertical disruptions, we have also used the plasma control system to achieve real-time disruption detection followed by gas puff mitigation.

General magnetohydrodynamic (MHD) stability considerations suggest that high triangularity, double-null discharges are attractive because of their high beta limits. Divertor designs for these were thought to be difficult for reactors because of the restricted space for the inner divertor components. However, our recent experiments have shown that balanced double-null discharges have almost no heat and particle flux to the inner strike points. Particle flux reductions of a factor of 5 and heat flux reductions of a factor of about 7 to 20 have been demonstrated [24,25]. These low heat and particle fluxes should substantially ease the inner divertor design problem.

A third theme in the DIII-D work in the past two years is detailed investigations of the edge pedestal and scrape-off layer (SOL). Detailed investigations of the width of the edge electron density barrier in DIII-D show that both plasma physics and atomic physics are important in setting this width [26-29]. Studies of ELM behavior indicate that ELM energy loss, normalized to the pedestal energy, decreases with increasing density owing to reduction of conducted heat flux. The convective transport of energy, measured as a drop in pedestal density, remains constant as a function of density [30]. SOL studies have shown that intermittent convective transport is an important particle transport mechanism in the region outside the separatrix [31-33].

2. HIGHER BETA LIMITS

2.1. Resistive wall mode stabilization

Our primary concept for an advanced tokamak includes both high power density, which means high β_T, and steady-state operation, which requires high bootstrap fraction for economical current drive. Both of these requirements demand operation at the highest β_N possible. One of the key instabilities which limits β_N is the external kink mode. Accordingly, one of the foci of our AT program is wall stabilization of the external kink [7–9].

As is summarized schematically in Fig. 2(a), the beta limit set by the external kink can be raised significantly from β^{nowall} to $\beta^{\text{ideal wall}}$ by the presence of a perfectly conducting wall near the plasma. This effect occurs because of the global structure of the kink mode, which exists both inside and outside the plasma. However, as is indicated in Fig. 2(b), the finite resistivity of most wall materials modifies this optimistic picture. The external kink now couples to the RWM, which can grow on a time scale τ_W, which is characteristic of the time needed for fields to penetrate the wall. This time constant is quite long compared to the usual kink growth time, which makes it possible to use active coils to compensate for the resistive effects of the wall; the effects of this feedback compensation are shown schematically in Fig. 2(b). In tokamaks with unidirectional beam injection, there is an additional stabilizing effect due to plasma rotation relative to the wall, which was first discussed by Bondeson and Ward [34,35]. As is shown in Fig. 2(c), if the rotation is sufficiently fast, the RWM is stabilized. Feedback stabilization and rotational stabilization can be combined to improve the overall stability.

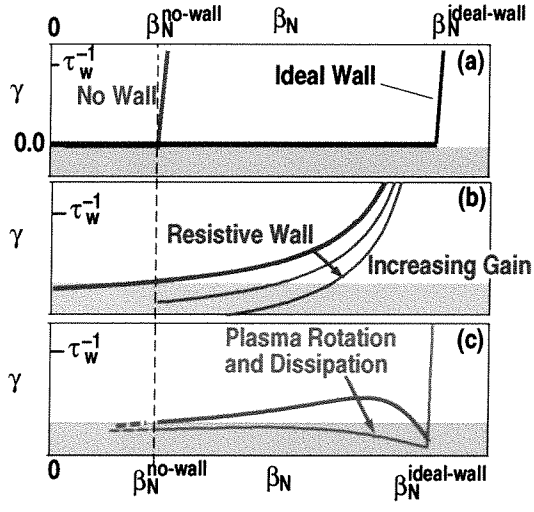

Fig. 2. Calculated growth rates of the external kink mode as a function of the normalized plasma pressure β_N. Shown are (a) stabilization of the external kink mode by an ideal wall, (b) stability of the RWM branch of the external kink mode for a wall with finite conductivity also showing the stabilization of the RWM by magnetic feedback with increasing amounts of feedback gain, (c) stabilization of the RWM by increased amount of plasma rotation and dissipation. The shaded region at the bottom of each box shows the stable region where $\gamma < 0$.

Initial attempts at rotational stabilization of the RWM showed that it was transiently successful but that the plasma rotation slowly dropped after the plasma beta crossed the no-wall beta limit [36]. This ultimately lead to beta collapse and, sometimes, disruption. A key insight here was provided by Boozer [37]

who proposed that, near marginal stability, the plasma has a resonant response to any non-axisymmetric external magnetic field component which has the same mode structure as the RWM. In other words, the RWM can resonantly amplify small external error fields and increase the drag on the plasma rotation when β_T is above the no-wall limit. If these external, non-axisymmetric fields are reduced, the drag is reduced and the plasma rotation can be maintained. Using the C-coil set on DIII-D to reduce the external error field, we have been able to sustain the plasma rotation and operate routinely above the no-wall beta limit. The most elegant way to determine the correct C-coil program to minimize the error field is to use the same feedback sensor and power supply system that was first developed for RWM stabilization [38,39]. As can be seen in Fig. 3, with a proper feedback algorithm, the plasma rotation can be sustained and the beta value raised all the way to the ideal wall beta limit. For these discharges, the ideal wall beta limit is approximately a factor of two above the no-wall beta limit. This demonstrates a substantial increase in the stable tokamak operating space.

As is shown in Fig. 4, preprogrammed C-coil currents which approximate the results of the feedback programming are also able to sustain the plasma rotation and allow operation above the no-wall limit. This demonstrates that the details of the magnetic feedback are not important for rotational stabilization. By adjusting the beta value through feedback control of the neutral beam heating system, we have produced sustained operation for up to 1.5 s, limited by duration of power supply operation; this is 10 τ_E or 300 τ_W. On the usual ideal MHD kink growth times, this represents essentially steady-state operation. Comparison of the rotational stabilization with predictions of the MARS code [40] shows qualitative agreement but more work needs to be done on the details of the plasma dissipation.

Feedback stabilization of the RWM has also been successfully demonstrated in cases where the rotation alone is insufficient to stabilize the mode [8]. Experimental results [41] are in good qualitative agreement with

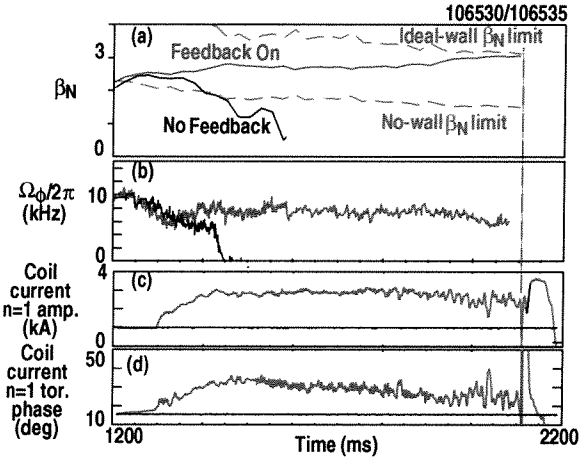

Fig. 3. Experimental achievement of high pressure plasma close to the ideal wall MHD limit using rotational stabilization of the RWM. Note that the ideal wall limit here is approximately twice the no-wall beta limit. Shown in (a) are traces of the plasma pressure (β_N) versus time in two discharges, one with and one without feedback to minimize resonant field amplification. The plotted ideal-wall and no-wall limits have been verified by the GATO code using the experimentally measured pressure and q-profiles. (b) The time evolution of the plasma rotation frequency near the q=2 surface for the two discharges; note the rapid drop in rotation for the no-feedback case after β_N crosses the no-wall limit. (c) The amplitude of the n=1 radial magnetic field supplied by the C-coil system; with no feedback, this current is preset to 1 kA. (d) The toroidal phase of the n=1 radial magnetic field supplied by the C-coil; without feedback, the preset value is 16 deg.

modeling predictions [42–44] that RWM stabilization is improved with radial magnetic field sensors inside the vacuum vessel wall as compared to radial field sensors outside the vessel wall and further improved with poloidal field sensors inside the vessel; these latter have faster time response and also do not couple to the field applied by the C-coil. A new set of twelve control coils inside the vacuum vessel is predicted [7,42,45] to allow feedback stabilization up to essentially the ideal wall limit even in the absence of rotation. These new coils will be operational for the 2003 experimental campaign.

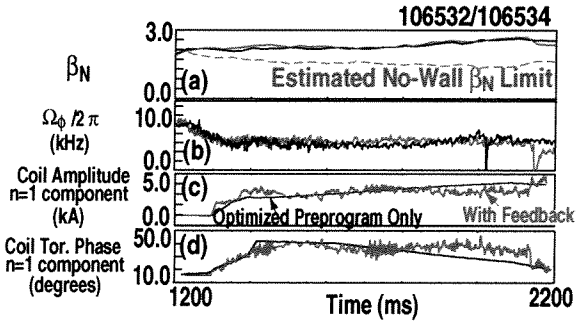

Fig. 4. Experimental achievement of a high β_N discharge using pre-programmed C-coil current showing that the details of the feedback are not necessary for rotational stabilization of the RWM. The red traces are with feedback and the blue is without. Shown in (a) is the plasma pressure β_N versus time; the dotted line in the graph shows the estimated no-wall β_N limit. Shown in (b) is the plasma rotation near the q=2 surface, in (c) the amplitude of the n=1 component of the C-coil current and in (d) the toroidal phase of that current.

The basic ideal MHD theory of the external kink, no-wall beta limits is in excellent agreement with experiment. By looking at the damping of the RWM at various beta levels, we have checked in detail that the calculated and measured no-wall beta limits agree [8]. In order to have a complete predictive understanding in this area, more work needs to be done on the theory of rotational stabilization, especially on the dissipation mechanism, and on feedback control in the presence of plasma rotation. Because rotation effects are always important in DIII-D, even in cases where rotation is too small for complete stabilization, our lack of quantitative understanding of rotational stabilization significantly affects all our detailed, quantitative theory-experiment comparison of wall stabilization. The most recent comparisons are summarized by Chu *et al.* [45].

2.2. Neoclassical tearing mode stabilization

Neoclassical tearing modes are magnetic islands destabilized and maintained by a helically perturbed bootstrap current and represent a significant limit to performance at higher β_p [46]. Theory predicts [47,48] that these confinement degrading islands can be reduced or completely suppressed by precisely replacing the missing bootstrap current in the island O-point with radially localized ECCD; this was first demonstrated in the ASDEX Upgrade tokamak [49]. The ECCD must be precisely located on the island for maximum effectiveness; misalignment of the current drive by only 2.5 cm from the proper location produces negligible stabilization. In order to routinely achieve this alignment, the DIII-D computerized plasma control system (PCS) has been programmed to feedback on the amplitude of the Mirnov probe signals in order to adjust the ECCD location for optimum suppression [12-14].

Since the initial stabilization of the (3,2) mode in sawtoothing discharges reported at the last IAEA meeting [50], we have now demonstrated that we can both stabilize the (3,2) mode and then increase the β_T value. As is illustrated in Fig. 5, ECCD suppresses the (3,2) mode even in the presence of large sawteeth and fishbones [14]. After the mode amplitude is essentially zero, the PCS no longer has the input needed for the real-time feedback and the location of the ECCD is held fixed. The neutral beam power is then programmed to increase; the beta increases 60% (20% higher than the peak before the onset of the NTM) before the mode reappears. The reappearance is due to the Shafranov shift of the plasma at higher beta, which moves the q = 3/2 surface about 2 cm away from the ECCD location; this reduces the ECCD stabilization substantially. There was not enough time left in the beam pulse on these shots for the PCS to go through another search and suppress cycle to adjust the ECCD location. We have now developed a method for the PCS to track changes in the q = 3/2 location even in the absence of the Mirnov signal so that, in the future, we can maintain the NTM stabilization as beta changes.

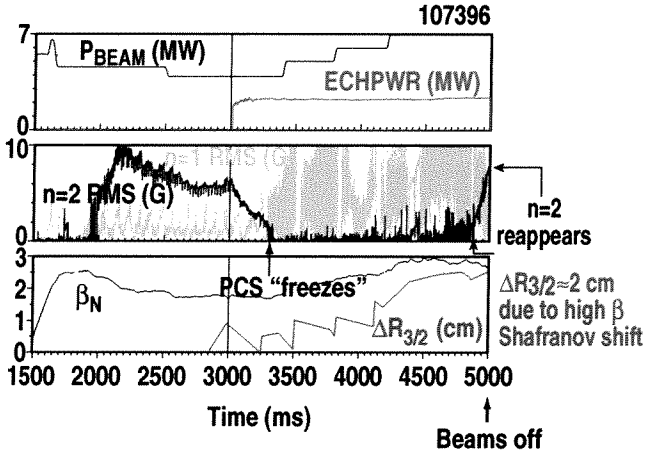

Fig. 5. Approximately 2.3 MW of ECCD is used to suppress an (m,n) = (3,2) NTM (shown by dark blue curve in central box) after which neutral beam power is raised to increase beta. β_N is increased by 60% despite the presence of large sawteeth and fishbone MHD oscillations (shown by light blue curve in central box). The NTM reappears at about 4900 ms because the Shafranov shift $\Delta R_{3/2}$ due to the higher beta has moved the q=3/2 surface where the NTM can exist about 2 cm away from the ECCD location.

Preliminary experiments have been done to apply the same NTM stabilization techniques to the (2,1) NTM [13,14]. As is shown in Fig. 6, complete suppression of a (2,1) NTM was obtained with 2.3 MW EC power. β_N was temporarily increased to about 3.5 to excite the NTM; complete suppression was achieved at β_N = 2.3 when the PCS adjusted the ECCD location to the optimum position. As is also shown in Fig. 6, ECCD 10 cm off the optimum had little effect. No attempt has been made yet to raise the β_T value after (2,1) NTM suppression.

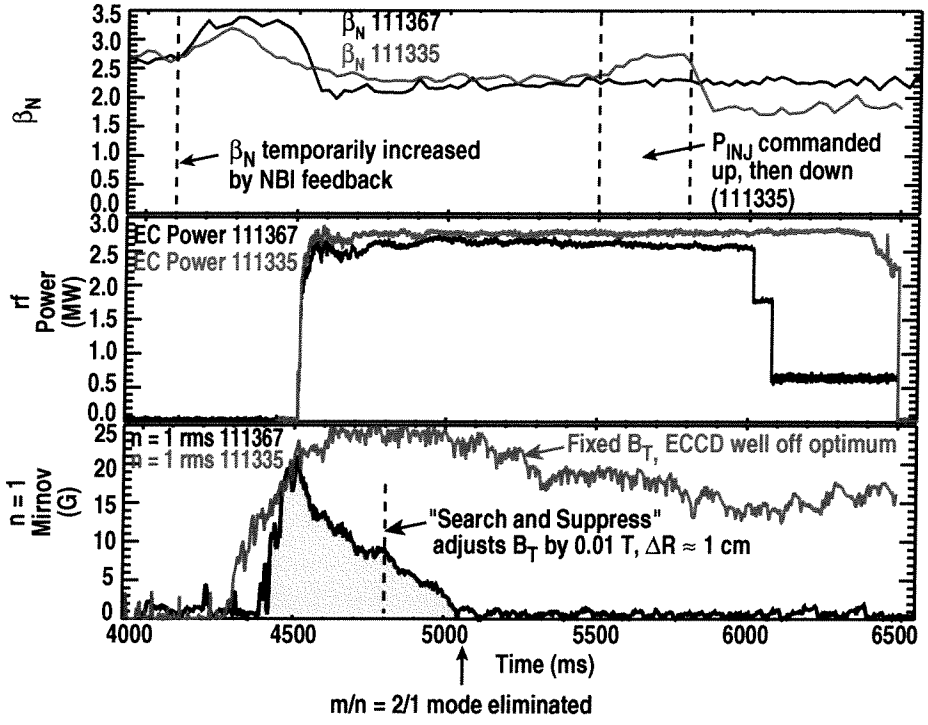

Fig. 6. Comparison of two shots demonstrating stabilization of the (m,n) = (2,1) NTM when the ECCD location is properly adjusted to suppress the mode. In both shots, neutral beam power is increased before 4500 ms to trigger the mode and then lowered again. The red trace in the bottom box with the ECCD 10 cm off optimum location demonstrates that this decrease in the beam power has little effect on the NTM amplitude. Shown in (a) is the normalized beta β_N, in (b) the power from the EC system, and in (c) the amplitude of the n=1 NTM at the Mirnov sensors mounted on the vessel wall. These shots are run using feedback control of the neutral beams so that the β_N time history matches a preprogrammed waveform. For this reason, β_N does not increase when the NTM is stabilized. The preprogrammed β_N waveform for the two shots differs in the region between the vertical dashed lines in (a).

3. PROFILE CONTROL

3.1. Current density profile control

In order to investigate optimum current profile shapes in machines like DIII-D where the pulse lengths are only a few current relaxation times τ_{CR}, shaping the current profile in the initial phase of the discharge remains an important tool. A standard technique to form broad or transiently hollow current density profiles is heating the plasma during the initial current ramp, thus decreasing the resistivity and slowing the current diffusion. Feedback control of the ECH during the current ramp has allowed a new level of control over this initial current density profile in DIII-D. As is shown in Fig. 7, by adjusting the requested T_e and ECH deposition location, a range of q-profiles can be obtained. This feedback control of T_e substantially increases the reproducibility of the initial current density profile, since small changes in initial plasma density no longer influence T_e. In addition, the same T_e time history can be obtained over a substantially wider range in density, essentially decoupling T_e and n_e and broadening the operating space. Replacing neutral beam with EC power also allows reduction in beam-produced particle input.

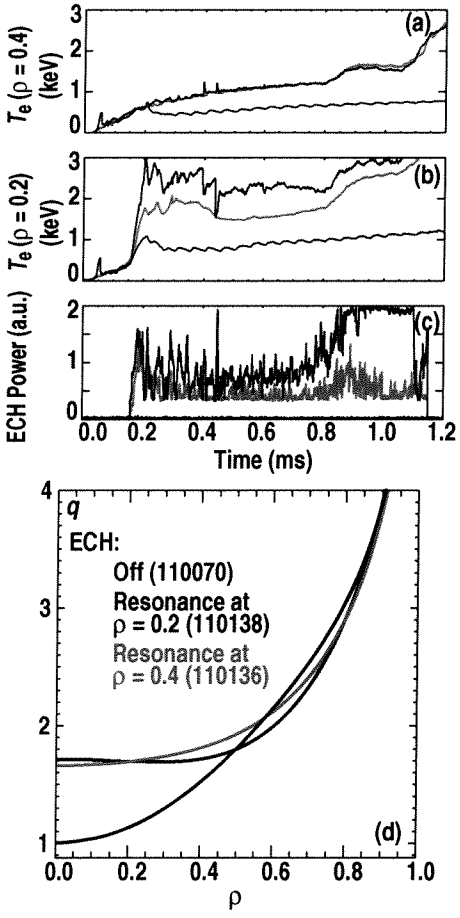

Fig. 7. Illustration of the effect of using T_e feedback with ECH to shape the q-profile at the end of the current ramp in several discharges. For the red and blue cases, ECH power was adjusted to match a preselected time history of the electron temperature at ρ=0.4. The black traces are for a no-ECH comparison case. For the blue curve, the ECH deposition was at ρ=0.2 while for the red case it was at ρ=0.4. (a) Electron temperature at ρ=0.4. (b) Electron temperature at ρ=0.2. (c) ECH power. (d) safety factor q versus normalized radius ρ at 1.1 s into each shot.

After the initial current profile has been set at the end of the current ramp, ECCD allows detailed control of the current density profile for the duration of the ECCD (2 s at present). In order to make best use of the available EC power, we have done extensive transport modeling in order to develop our experimental plans. This coupling of detailed modeling and

experiment has created a great improvement in the way we conduct these experiments. Accurate modeling requires a verified theory to allow computation of the ECCD. We have performed extensive theory-experiment comparisons over the past several years [51,52]. As is illustrated in Figs. 8 and 9, these investigations show excellent agreement between the measured ECCD and the predictions of quasi-linear theory embodied in the CQL3D code [53]. One key aspect of this agreement is the strong beta dependence of ECCD efficiency for the off axis current drive needed for AT plasmas with hollow current profiles. The measurements in Fig. 9 show we have achieved the ECCD efficiency needed to carry out our planned AT developments in the next several years.

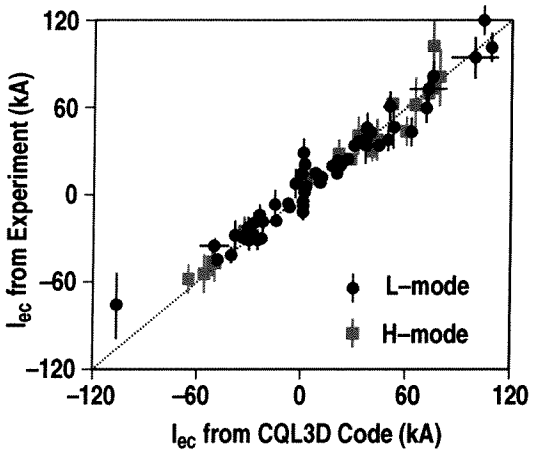

Fig. 8. Comparison of measured and predicted ECCD over a range of parameters for both L-mode (blue circles) and H-mode (red squares) plasmas. The predictions are from the CQL3D code using the measured experimental profiles as input.

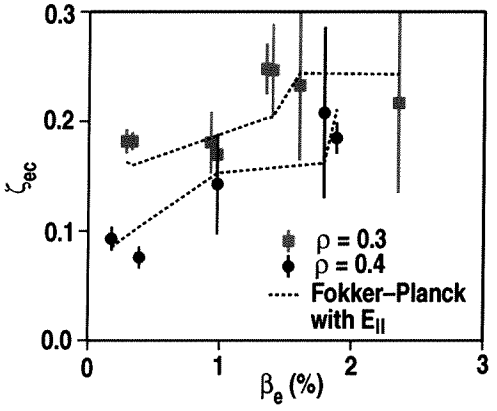

Fig. 9. Measured dependence of the dimensionless ECCD efficiency on the local electron beta for ECCD deposited at ρ = 0.3 (red squares) and ρ = 0.4 (blue circles) for EC injection with parallel index of refraction $N_{||}$ = 0.4 and a poloidal heating location 85 deg, near the top of the flux surface. The ECCD efficiency ζ_{ec} is given by (e^3/ε_o^2) $(I_{ec}Rn_e/P_{ec}T_e)$, where I_{ec} is the current driven, R is the major radius and P_{ec} is the EC power used. The theoretical predictions from the CQL3D code are shown as dashed lines.

Based on our modeling, we have carried out initial, integrated AT experiments which combine high beta operation (β_N = 2.8, β_T = 2.9%) at high q_{min} ~ 2, good plasma confinement with $H_{89} \geq 2.5$ and high non-inductive current fraction (about 90%). In these discharges, ECCD at ρ = 0.4 is integral in producing negative central magnetic shear and helping to form a weak internal transport barrier for both electrons and ions. This core-barrier formation with ECCD was not anticipated in the modeling. It is in distinct contrast to the typical observation of confinement deterioration when using ECH/ECCD in plasmas with $T_i/T_e >> 1$.

Figure 10 shows the temporal evolution of a representative shot of this class of discharges. An H-mode is induced early in the current ramp; coupled with neutral beam injection (NBI), this slows the penetration of the current leading to a slightly negative central magnetic shear profile with $q_{min} > 2.5$ at 1.5 s into the discharges. β_N is then increased by feedback control of the NBI to β_N ~ 2.8 and held there for the remainder of the discharge. Application of 2.5 MW ECCD at 1.5 s increases the negative magnetic shear by raising q(0) to about 5 while q_{min} remains ≥ 2 for

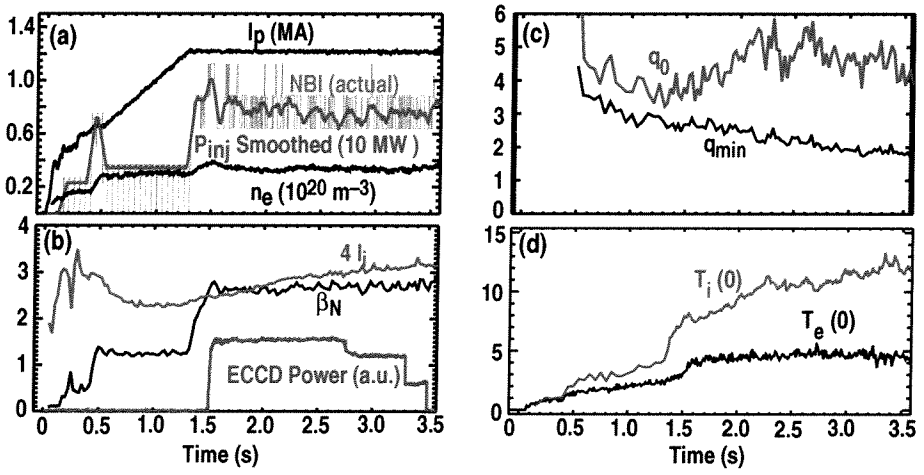

Fig. 10. Plasma parameters versus time for AT plasma shot 111203, which uses ECCD to generate negative central magnetic shear and sustain an internal transport barrier for nearly 2 s. (a) Plasma current (in units of MA), neutral beam injected power (in units of 10 MW) and line-averaged density (in units of 10^{20} m^{-3}); (b) β_N, plasma internal inductance ℓ_i and EC power; (c) minimum and central safety factors; and (d) central electron and ion temperatures.

the 2 s duration of the ECCD pulse. Comparisons with cases with radially launched ECH (hence no current drive) indicate that the current profile modification is almost entirely the result of the application of ECCD as the ECH case and an NBI only case show little difference in the q-profile. Analysis indicates that ECCD generates a total current of about 130 kA, which is consistent with the CQL3D prediction. The remainder of the plasma current is provided by neutral beam current drive (~25%), bootstrap current (~55%) and Ohmic current (~10%). Accordingly, the non-inductive current is about 90% of the total current.

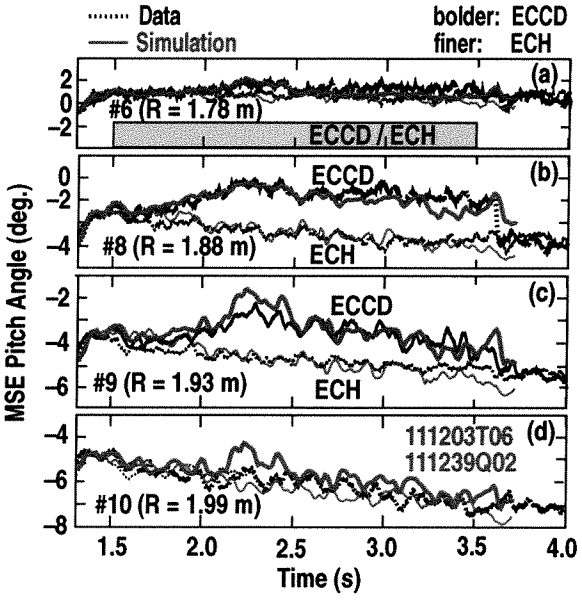

Fig. 11. Comparison of the measured pitch angle from the MSE system with those calculated from the TRANSP code for the high performance, ECCD shot shown in Fig. 10. Each box shows the pitch angle at a different radius value indicated on the figure. There are two cases shown, one with ECCD and one with radial launch ECH, which produced no current drive. Note the excellent agreement between the calculations and the measurement. Note also that the measurements show the spatial localization of the ECCD expected theoretically. ECH and ECCD are on from 1.5 to 3.5 s.

As is shown in Fig. 11, there is excellent agreement between the changes in the internal magnetic field line pitch measured by the motional Stark effect (MSE) diagnostic [54] and the results of the current drive modeling carried out using the measured profiles. The comparison with radial launch ECH cases shows the localized nature of the ECCD and again illustrates the good agreement between ECCD theory and experiment.

3.2. Plasma pressure profile control

Pressure profile control tools are also important for AT plasmas since, in shaped plasmas, broad pressure profiles generally lead to higher MHD beta limits and higher fusion reactivity [55]. The discovery of core transport barriers in the early 1990s showed that it was possible to create a variety of core pressure profiles, depending on the exact plasma conditions used. Initial work on core transport barriers showed that manipulation of the core E×B via neutral beam injection and altering the Shafranov shift through negative central shear q-profiles were important methods of creating core transport barriers. Our recent experiments have shown that ECH and ECCD can also be used as transport barrier control tools.

As was mentioned in the previous section, ECCD into one type of AT plasma has altered the q-profile and triggered a weak core transport barrier in all four transport channels: electron and ion thermal transport, particle transport and angular momentum transport [15]. This barrier is not seen in the radial launch ECH or pure NBI comparison cases; accordingly, we conclude that the change in the q-profile was the important factor. Preliminary analysis using the GKS gyrokinetic stability code [56] indicates that both E×B shear stabilization and Shafranov shift (α) stabilization are important in these discharges. The presence of Shafranov shift effects may be particularly important, since Shafranov shift stabilization reduces turbulence growth rates over a wide range of spatial scales which affect both electrons and ions while E×B shear affects the longer wavelength turbulence which primarily affects ions.

Although the confinement improvement owing to core barrier formation can be beneficial, in some cases the profiles can become too peaked. One example of this is the very peaked density profiles produced in QDB discharges which lead to quite peaked impurity density profiles [17]. Injecting about 2 MW of ECH or ECCD into already established core barriers in the QDB discharges substantially broadens the density profile, as is shown in Fig. 12. This is probably the same ECH effect on density which has been seen for decades in tokamaks [57]. The most dramatic results are seen with EC resonant at $\rho = 0.2$; weaker effects over a somewhat broader region are seen with injection at $\rho = 0.4$. Accordingly, it appears that we can tailor the effect by altering the EC deposition location. As is shown in Fig. 13, this change in density profile alters the radial profiles of the high Z impurities, which go from moderately peaked to essentially flat.

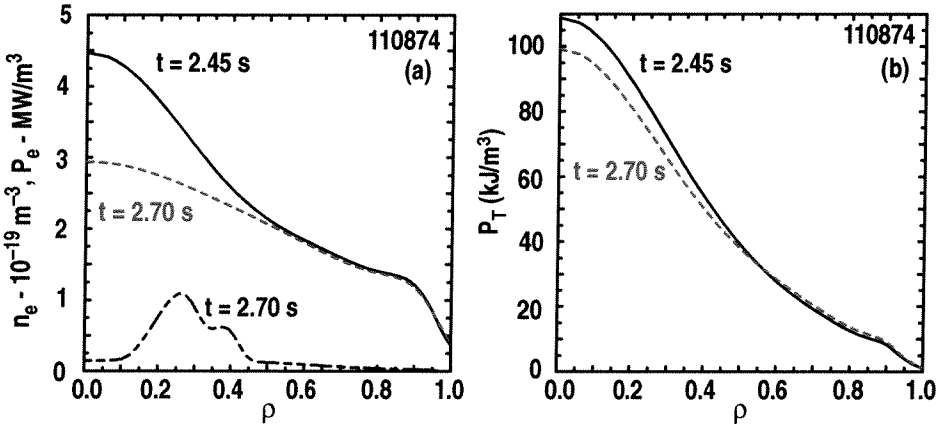

Fig. 12. Comparison of the (a) electron density and (b) total pressure profiles in a QDB discharge with and without ECH. The ECH is used in ECCD configuration at a nominal deposition radius of ρ = 0.2. Calculated EC power deposition profile is also shown by the dashed line at the botton of the figure in (a). Note the substantially broader density profile and slightly broader pressure profile with ECH. Plasma conditions are 1.3 MA plasma current, 2.0 T toroidal field, 2×10^{19} m^{-3} line averaged density in an upper single null divertor with divertor cryopumping.

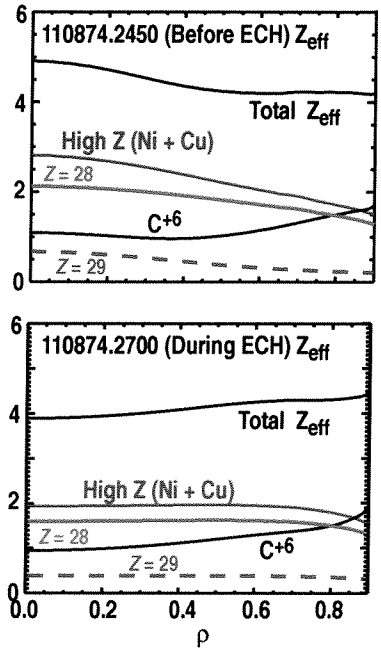

Fig. 13. Comparison of nickel and carbon profiles in the same discharge as shown in Fig. 12. The profiles are significantly flatter at the time when ECH has flattened the density profile.

4. IMPROVED OPERATING SCENARIO FOR ITER

A key figure of merit in the design of burning plasmas devices is the fusion gain, given by fusion power divided by heating power. The fusion gain of a burning plasma system can be related approximately to $\beta_T \tau_E$, which is proportional to $\beta_N H_{89}/q_{95}^2$. As is shown in Fig. 14, we have demonstrated $\beta_N H_{89} = 6.5$, $\beta_N H_{89}/q_{95}^2 \cong 0.4$ and $q_{95} = 4.2$ for up to 6.5 s (36 τ_E) with the duration limited by hardware constraints. Other shots show $\beta_N H_{89} = 7$ and $\beta_N H_{89}/q_{95}^2 \cong 0.4$ at $q_{95} = 4.4$ for about 6.3 s, again limited only by hardware constraints. These times are about two current relaxation times τ_{CR}. These cases match the $\beta_N H_{89}/q_{95}^2$ value of the ITER design but at a q_{95} well above the ITER value of 3. The increased normalized performance is due to both higher β_N and H_{89} than anticipated for low-q ELMing H–mode. The discharges are stationary on the thermal, resistive and wall equilibration time scales. These discharges utilize feedback controlled density and beta values to achieve a stationary state in which a small (3,2) tearing mode keeps q_{min} just above unity, preventing sawteeth and fishbones. We believe the presence at the (3,2) mode is an essential part of this type of operation [18].

The operational β_T limit in these discharges at present is the onset of (2,1) NTMs. Because the classical mechanisms producing the NTM seed island (i.e. sawteeth and fishbones) are absent in these discharges, they can be operated at much higher β_N than conventional, sawtoothing, ELMing H-modes. Experimentally, these discharges can be operated at the no-wall beta limit [18]. Initial attempts at using RWM feedback in this class of shots have demonstrated some modest increase in rotation, suggesting that the plasmas are slightly above the no-wall limit. Experiments on stabilization of the (2,1) NTM with ECCD in these plasmas are planned for the future.

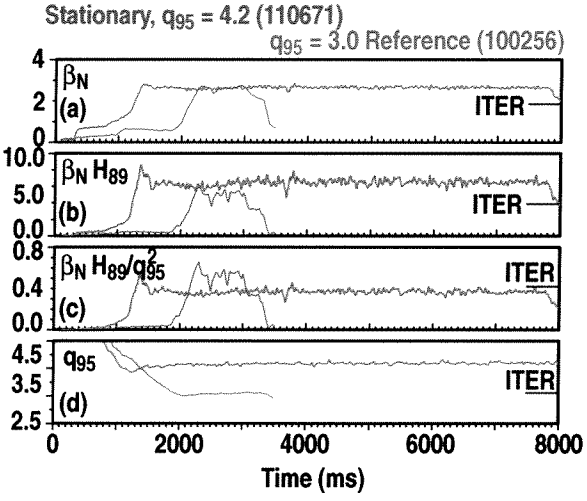

Fig. 14. Time history of plasma parameters comparing a stationary plasma at $q_{95} = 4.2$ with a reference discharge at $q_{95} = 3$. (a) Normalized beta, (b) normalized beta multiplied by H-factor based on ITER89P scaling, (c) fusion gain parameter, and (d) safety factor at the 95% flux surface. Indicated by a short line at the edge of each box is the ITER design value. Note that the fusion gain parameter matches the ITER design value while q_{95} is significantly higher. Stationary duration of 6.5 s is 36 τ_E or two times the current relaxation time τ_{CR}.

As is shown in Fig. 15(a), thermal transport in these discharges is much below what one would expect, scaling the single-fluid

hermal diffusivity χ_{eff} from q_{95} = 3 reference cases. Empirical scalings suggest that $\chi_{eff} \sim q^{1.4}$ while nondimensional scaling results give $\chi_{eff} \sim q^2$ [58]. Given these scalings, the near equality of the χ_{eff} values for the q_{95} = 4.5 and q_{95} = 3.0 discharges shown in Fig. 15(a) is quite surprising. Predictive transport calculations utilizing the GLF23 code [59-61] shown in Fig. 15(b) demonstrate that the predicted T_e and T_i profiles agree well with the experimental results in the plasma core. The GLF23 results indicate that the reduction in transport is due to a combination of $T_i/T_e > 1$ and sufficient E×B shear, both acting to reduce turbulent transport. These results also indicate that turbulence is not completely suppressed, which is consistent with the ion thermal diffusivity χ_i being significantly larger than the neoclassical value. These GLF23 results are one example of our broader effort to develop a predictive understanding of transport [61].

The results in Fig. 14 have been achieved at relatively low density in discharges with $T_i/T_e > 1$. Because these conditions are a concern for extrapolation to burning plasmas, experiments have been conducted exploring higher density operation in the range from n_e/n_{GW} = 0.3 to 0.5. Here, n_{GW} is the Greenwald density [62]. Over this range, confinement quality decreases only slightly while ion collisionality ν_i, effective charge Z_{eff}, and T_i/T_e move much closer to the ITER design values. The trends indicate that by increasing the density to n_e/n_{GW} = 0.7, ν_i and T_i/T_e values consistent with the ITER values should be achieved [18].

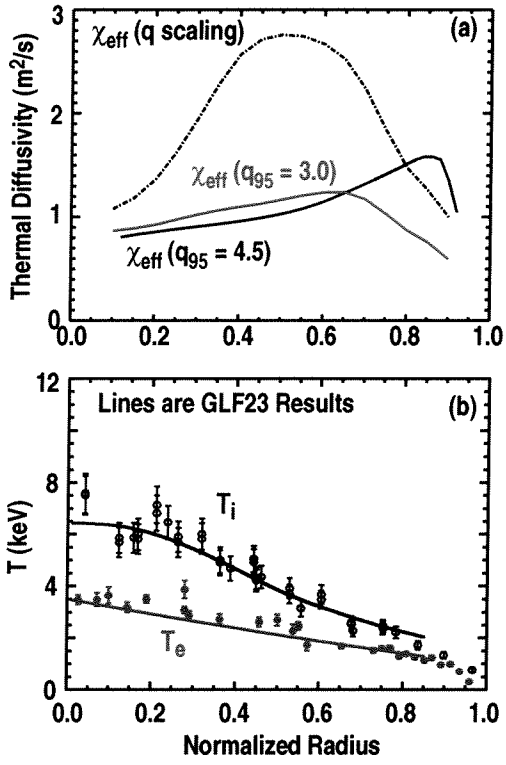

Fig. 15. (a) Comparison of the experimentally inferred single fluid thermal diffusivity χ_{eff} at 5.7 s for shot 104276, a stationary, high q_{95} discharge similar to that in Fig. 14 with the χ_{eff} averaged over the range of 2.9 to 2.95 s from shot 100256, a q_{95} = 3 reference shot. Also shown, as an illustration of possible q-scaling, is the χ_{eff} from 100256 multiplied by the ratio of the local q values in the two shots. Plasma conditions for 104267 are I_p = 1.2 MA, B_T=1.7 T and line averaged density 3.7×10^{19} m^{-3} while the corresponding numbers for shot 100256 are 2.0 MA, 1.6 T and 1.1×10^{20} m^{-3}. (b) Comparison of measured electron (closed circles) and ion (open circles) temperature profiles for shot 104276 at 5.71 s with the predictions from the GLF23 code. These show excellent agreement. For the calculation, the experimental temperatures at ρ = 0.85 were used as boundary conditions; the measured electron density profile and the standard model calculations for the heat sources were used as inputs.

5. GENERAL TOKAMAK IMPROVEMENTS

5.1. Quiescent H-mode

The pulsed heat and particle loads to the divertor caused by Type I ELMs pose significant design issues for divertor components in future burning plasma devices. Because of its improved energy confinement, there is general agreement that H-mode plasmas will be used in these devices. Accordingly, the world fusion community is seeking solutions to the Type I ELM heat load problem. One solution discovered on DIII-D is the quiescent H-mode, which has the H-mode edge transport barrier but does not exhibit ELMs [17,19,20]. An example of a fairly long pulse QH-mode plasma is shown in Fig. 16. In this case, the quiescent phase lasts about 3.8 s or about 25 τ_E. In standard ELM-free H-mode, particle confinement time is so good that the density rises monotonically until either an ELM occurs or the plasma suffers radiative collapse. As can be seen, QH-mode can be run with basically constant density and radiated power, owing to the presence of an edge electromagnetic mode, called the edge harmonic oscillation (EHO), which increases the edge particle transport [19,20]. When the EHO starts from a standard ELM-free phase, there is a clear correlation between decreased plasma density and increased divertor D_α, indicating deuterons have left the main discharge and gone into the divertor [20]. Measurements of the heat load to the divertor show that the heat load profiles are broader than those for standard ELMing H-mode [17].

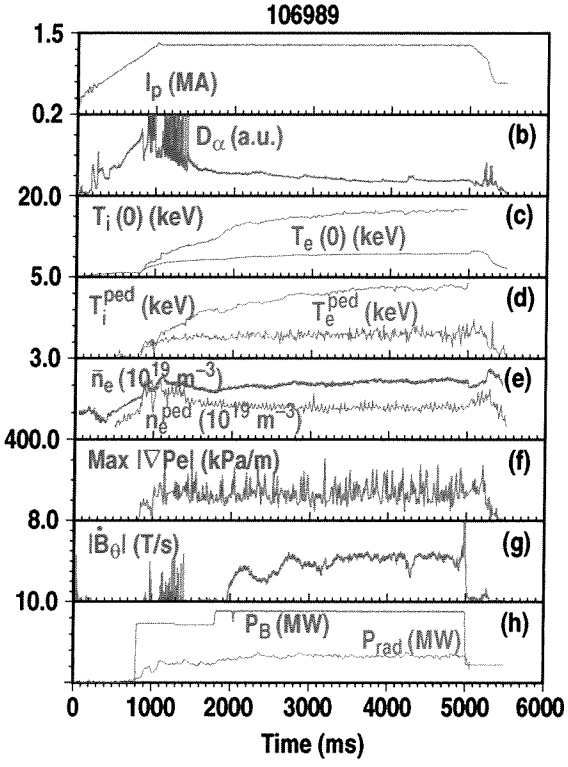

Fig. 16. Time history of plasma parameters for a QH-mode shot. (a) Plasma current, (b) divertor D_α emission, (c) central ion and electron temperatures, (d) pedestal ion and electron temperatures, (e) line-averaged density and H-mode pedestal density, (f) maximum of the edge electron pressure gradient, (g) dB_θ/dt from Mirnov loop at vessel midplane, (h) total injected neutral beam power and total radiated power. As is indicated by the D_α emission, this shot is in quiescent H-mode for 3800 ms. Toroidal field is constant at 2.01 T until 5000 ms in this shot.

At present, QH-mode has been seen over a reasonable parameter space [19,20] but has always been done with neutral beam injection counter to the plasma current. QH-mode has been seen with input powers as low as 3 MW;

maximum input power used to date is 13.5 MW. We have seen quiescent H-modes over entire range of triangularity ($0.16 \leqq \delta \leqq 0.75$) and safety factor q_{95} ($3.4 \leqq q_{95} \leqq 5.8$) explored to date. Most of our work has been done with plasma current in the range $1.0 \leqq I_p$ (MA) $\leqq 2.0$ and toroidal field in the range $1.8 \leqq B_T$ (T) $\leqq 2.1$. We also have quiescent H-mode examples at I_p = 0.67 MA and B_T = 0.95 T. Pedestal densities are in the range of 1×10^{19} m^{-3} to 6.5×10^{19} m^{-3}. Although the EHO has been seen in co-injected discharges, the quiescent H-mode has not. Future experiments are planned to expand the parameter space further.

5.2. Disruption mitigation

Experiments on DIII-D have demonstrated that the impact of disruptions on first wall or in-vessel components can be greatly reduced by the injection of noble gas using a high pressure gas jet [21-23]. Modeling indicates this technique extrapolates well to future burning plasmas experiments. Recent experiments on DIII-D have shown that this technique will mitigate three major disruption effects in future devices: divertor surface melting/ablation by plasma heating, mechanical stress from halo currents and the production of relativistic, runaway electrons.

The basis of this technique is the injection of a noble gas (neon or argon) into the plasma as is shown in Fig. 17. The gas jet is found to penetrate to the central plasma at the gas sound speed (300 to 500 m/s) owing to its high density (>10^{24} m^{-3}) and high pressure (>20 kPa). The jet increases the atom/ion content of the plasma by a factor of 50 in several milliseconds. As a result, the plasma energy is dissipated uniformly on the vessel wall by UV radiation from the injected impurity. The conducted heat flux to the divertor is 2% to 3% of the plasma kinetic energy, compared to 20% to 40% for non-mitigated disruptions. The plasma remains well centered in the vessel while the current decays rapidly in the cold, resistive plasma. Runaway electrons are well controlled by the gas jet injection, in contrast to mitigation attempts with cryogenic argon pellets. The large neutral density of the gas jet effectively suppresses the runaways.

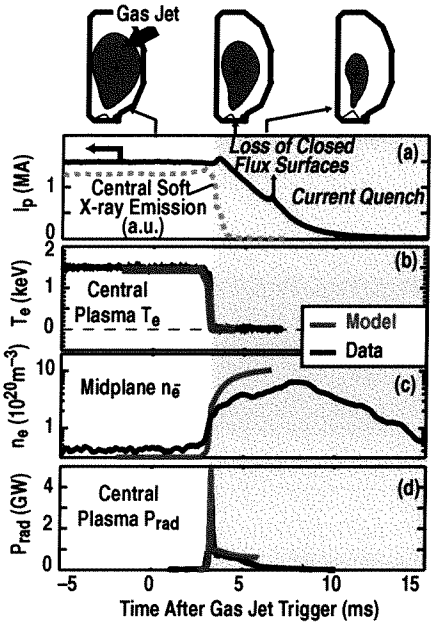

Fig. 17. Time history of plasma parameters across a disruption mitigated by neon gas injection. (a) Plasma current and central soft x-ray emission, (b) central electron temperature, (c) midplane line averaged density and (d) radiated power from the core plasma. Plasma shape at various times is shown within the vacuum vessel outline at top of figure. Overlaid in red in (b,c,d) are the results of the physics model of the disruption, showing excellent agreement. Note that, since the dense gas quenches fast electrons, the plasma current falls monotonically without the long plateau characteristic of runaways.

The type of disruption which can potentially do the most damage is the so-called vertical disruption event (VDE) in which plasma position control is lost and the plasma moves rapidly towards the divertor X-point. These can induce substantial, poloidally and toroidally asymmetric halo currents in the vacuum vessel. DIII-D has demonstrated real time detection and mitigation of VDEs using the plasma control system. In these experiments, vertical position control was deliberately disabled at a chosen time during the discharge. Using an independent detection system to determine the vertical shift, the PCS triggered the high pressure gas jet when the vertical position had moved by a preset amount between 2 and 10 cm. Compared to a VDE with no mitigation, the toroidal peaking factor for the halo current was reduced from 2 to 1.1 while the magnitude of the peak poloidal halo current was cut in half.

Based on physical models benchmarked against the DIII-D experimental data, it appears that this technique extrapolates favorably to future burning plasma experiments. Along with techniques to operate the discharge away from disruptive limits, gas jet mitigation should substantially improve design flexibility and operational reliability of next-step tokamaks.

5.3. Balanced double-null discharges

Both MHD stability considerations and operational experience suggest that high triangularity double-null discharges have significant performance advantages. For example, the discharge in Fig. 1 has this shape. Plasmas with this shape are not usually considered for burning plasma experiments because of the engineering difficulties related to 1) the magnetic field coil set needed to make this shape and 2) the difficulty in designing the divertors with their inner legs up against the center post. For the divertor, some designers have assumed that the heat and particle flux to the inner strike points for a balanced double-null plasma would be similar to those seen at the inner strike point in single-null divertor discharges; it would be difficult to find space on the centerpost for components to handle these loads. However, as is shown in Fig. 18, the particle flux to both inner strike points is quite low for the balanced configuration. The particle flux at the inner strike point is about 0.2 times that at the outer strike point while the heat flux at the inner strike point is 0.05 to 0.15 times that at the outer strike point [24,25]. These low heat and particle fluxes should substantially ease the design of the inner leg divertor components for double null discharges. These results are also consistent with measurements over the past decade which suggest that the ELM heat and particle fluxes originate primarily at the outer midplane of the plasma [63].

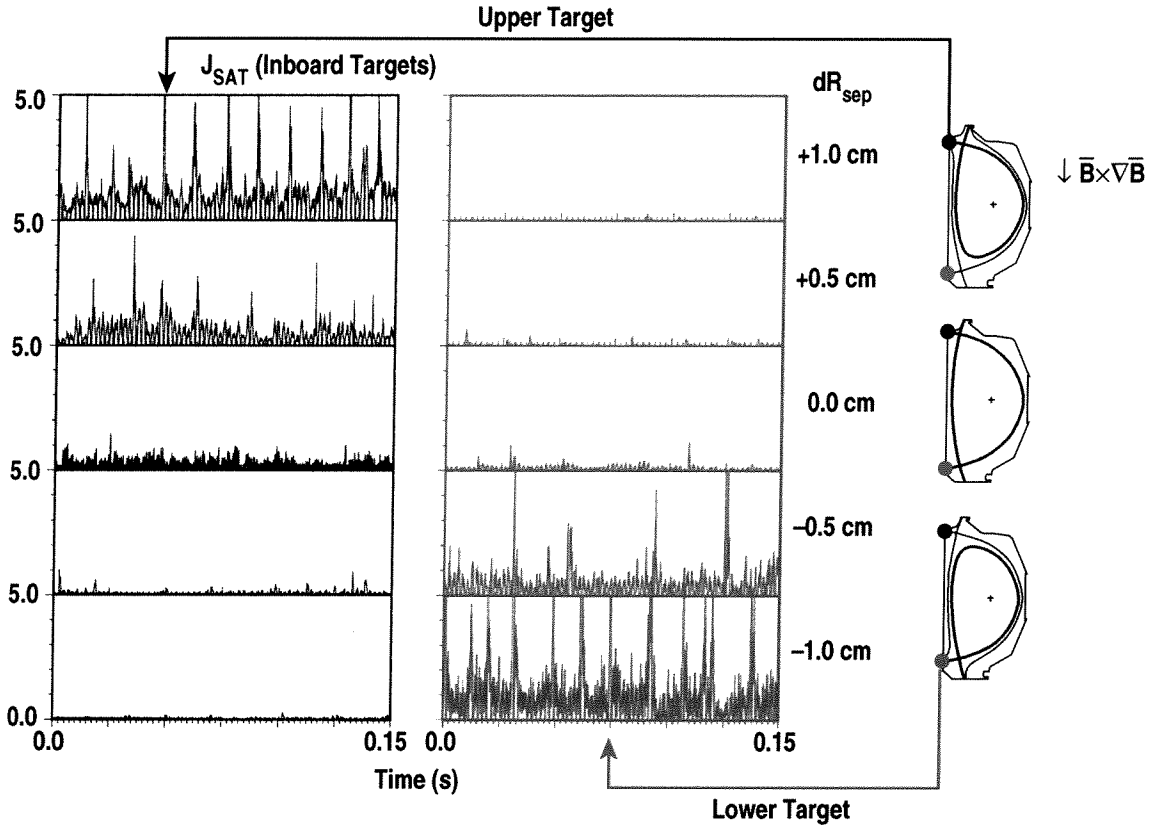

Fig. 18. Ion saturation current to Langmuir probes at the inner divertor strike points at the top and bottom of the plasma for a sequence of conditions where the plasma is changed from upper single null through balanced double null to lower single-null conditions. Note that for the balanced condition, the ion saturation current is small on both inner strike points simultaneously.

6. EDGE AND SCRAPE-OFF LAYER STUDIES

6.1. Edge pedestal studies

Experimental observations [64-66] and theoretical modeling [60] both show that the H-mode pedestal parameters in a given discharge have a substantial impact on the performance of the core plasma. Accordingly, developing a predictive understanding of the pedestal parameters is quite important. In ELMing discharges, the pedestal height can be determined from MHD stability calculations [67,68] once the width of the edge transport barrier is known. Determining the physics which sets this width is, consequently, a key issue.

Recent pedestal studies on DIII-D provide evidence that the width of the edge density barrier depends on both plasma physics and atomic physics [26-29]. The atomic physics includes the characteristics of the fueling neutrals; the plasma physics includes both the particle and energy transport. This evidence is based on a strong correlation between the width of the H-mode density barrier and the neutral penetration length. This correlation is obtained by comparing experimental edge n_e profiles to the predictions of a simple analytic model based on the coupled continuity equations for the electrons and the neutrals. Benchmarking of this model against the more sophisticated fluid neutrals model in the UEDGE boundary modeling code [69] shows that the analytic model gives very similar results to UEDGE. These results support the use of the analytic model to study trends in the plasma, despite the fact that the analytic model treats the neutral transport in a very simple way.

In its range of validity, the predictions of the analytic model are consistent with a number of DIII-D measurements: 1) Ohmic, L-mode and H-mode edge density profiles are predicted to have a hyperbolic tangent shape, consistent with the measurements. 2) The model predicts that the density barrier width decreases as pedestal density $n_{e,ped}$ increases. The widths tend to show some deviation from a strictly monotonic trend with pedestal density. This deviation is modeled as a transition from neutrals which are primarily at the Frank-Condon energy to neutrals equilibrated with the plasma ions via charge exchange. 3) For reasonable values of the model parameters, the model quantitatively predicts the experimental widths of the edge n_e profile. 4) As is shown in Fig. 19, the model predicts the maximum edge n_e gradient in reasonable quantitative agreement with experiment. The model does not distinguish between Ohmic, L-mode and H-mode cases; accordingly, as is seen experimentally, profiles with the same value of the pedestal density should have the same gradient. However, it is necessary to apply much higher gas injection rates in the Ohmic and L-mode cases to match the H-mode pedestal density, as is expected for the larger particle transport rates in the former cases. 6) The model nicely

explains the typical temporal history of the density profile across the L to H transition where we observe the width of the steep gradient region decreasing while the pedestal density increases. This phenomenology can be explained by a reduction of the particle diffusion coefficient with the particle source remaining unchanged (or increasing). The simplicity of the neutral transport model restricts the range of validity to electron temperatures from 0.02 to 0.3 keV.

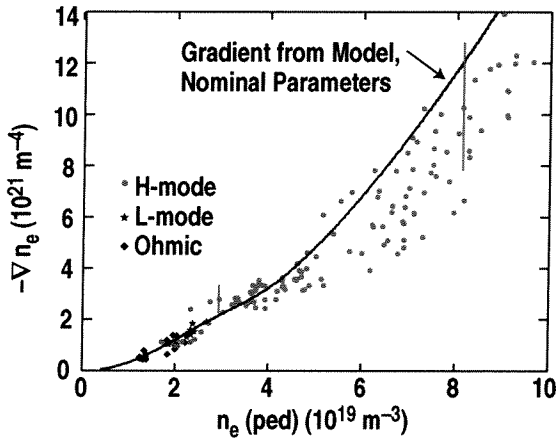

Fig. 19. Maximum edge electron density gradient versus the pedestal density for Ohmic, L-mode and H-mode conditions compared to the predictions of the analytic model of the edge density profile. The error bars reflect the scatter of results from several Thomson scattering measurements under nominally identical conditions. Note that for pedestal densities around 2×10^{19} m^{-3}, there are Ohmic, L-mode and H-mode points which overlap, showing that the gradient is the same for the same pedestal density independent of the operating mode.

6.2. ELM energy loss

In future burning plasma devices, ELM heat pulses to the divertor target plates must be maintained below a critical threshold to avoid unacceptable ablation [70,71]. Estimates show that this threshold for ITER is equivalent to loss of about 6% to 12% of the pedestal energy, which is computed by multiplying the pedestal energy density by the plasma volume. We are investigating whether this criterion can be met in discharges with standard, Type I ELMs, which are the baseline scenario, for example, for ITER. Type I ELMing regimes satisfying this constraint have been observed in DIII-D and other devices when operated at high density [72,73].

As is discussed by Leonard *et al.* [30], the ELM energy loss measured by Thomson scattering can be divided into a conductive and convective part. As is illustrated in Fig. 20, the convected energy loss varies little with density while the conducted part decreases approximately linearly as density increases, dropping to near zero at $n_{e,ped}/n_{GW} \cong 0.7$. The reduction in overall ELM energy loss with increasing density correlates well with the structure of the most unstable mode calculated by the ELITE code [67,68]. The mode width is smaller at higher density because higher collisionality reduces the edge bootstrap current and because the width of the edge pedestal is reduced. The ELM size at the highest $n_{e,ped}/n_{GW}$ would be acceptable in larger burning plasma devices. However, such devices would operate at significantly lower collisionality than the DIII-D cases, which could result in larger ELM heat pulses. In addition, as discussed in the last section, the physics governing the width of the steep edge gradient region is uncertain. Accordingly, model development benchmarked with further careful experiments will be required to reliably predict the ELM energy loss in a future burning plasma tokamak.

6.3. Intermittent SOL transport

Intermittent, bursting transport has been seen in the edge plasma of a number of devices (see discussion in [32]). Intermittent plasma objects (IPO) featuring higher pressure than the surrounding plasma and responsible for ~50% of the $E \times B_T$ radial transport are observed in the edge and SOL of the DIII-D tokamak in both H-mode and L-mode [31–33]. The intermittent transport is convective in nature and potentially enhances radial transport over diffusion. The skewness of Langmuir probe and beam emission spectroscopy data suggest IPO formation at or near the separatrix and exhibit the formation of hole-IPO pairs. In L-mode, the radial transport is sufficient to produce flat far SOL density profiles under some conditions. In H-mode, the particle content of the bursts is considerably smaller than in L-mode. The difference in the H-mode and L-mode radial particle fluxes is shown in Fig. 21. In L-mode, the particle density of the IPOs at the separatrix is an approximately constant fraction of the local plasma density, typically 50% to 70% of the local time-averaged density. The IPOs thermalize within about 1 cm of the separatrix consistent with models in which the parallel electron thermal transport is much faster than the particle transport.

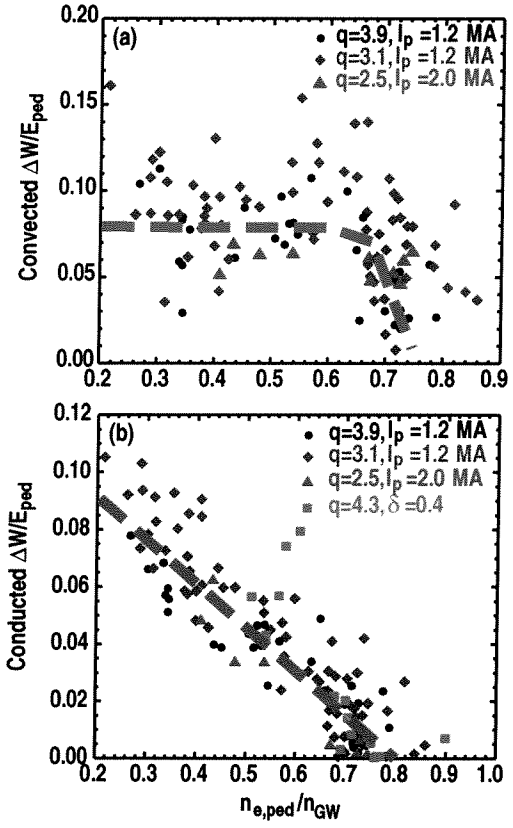

Fig. 20. (a) The normalized convected ELM energy loss as determined from a time history of Thomson scattering measurements versus the pedestal density normalized to the Greenwald density. The ELM energy loss is normalized to the pedestal energy. Using this normalization, the data from the four different conditions indicated appear to be part of one data set. (b) The normalized conducted ELM energy loss versus the normalized pedestal density. Dashed lines have been added in each box to guide the eye.

The IPOs appear at a rate of approximately 5×10^3/s and conditional averaging of the Langmuir probe data reveals that they are positively charged. The net charge gradually decays as the IPOs move from the separatix to the wall. The related electric field results in poloidal electric fields of up to 4 kV/m, which propel the structures radially with $E \times B_T/B^2$ speeds of 2.6 km/s near the separatrix and about 0.33 km/s near the vacuum vessel wall. The structures move poloidally at speeds of up to 4.5 km/s near the separatrix, slowing down towards the wall as they shrink in radial size from 2 cm to 0.5 cm. All this behavior is in semi-quantitative agreement with a recently developed model of the IPO [74,75]. Initial modeling with the BOUT code has also produced effects which look like the IPOs [76].

These results suggest that, in some cases, an additional effect exists above simple diffusion to produce particle flux to the vacuum vessel wall; this could affect recycling and impurity generation. The significance of these results for future machines depends on the relative ratio of IPO cross field transport and ELM-induced transport. Especially if the ELMs behave as a giant version of the IPO, then there will almost certainly be extra particle flux to the vessel wall.

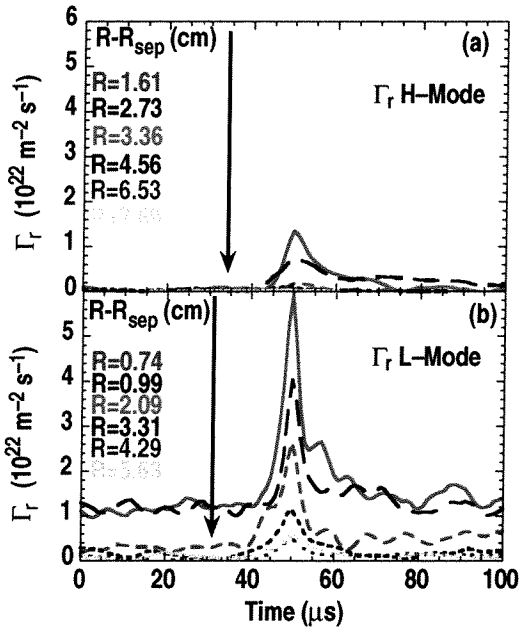

Fig. 21. Conditional averaging results showing the intermittent particle flux for L-mode and H-mode conditions. Data from different radii are superimposed, those from near the separatrix at the top and those from the far SOL at the bottom in each box, as the arrows indicate. The corresponding radii are given in each box. As can be seen, the intermittent particle flux in L-mode is significantly larger than in H-mode.

7. CONCLUSION

We have made significant progress in developing the building blocks needed for AT operation:

(1) We have substantially increased the MHD stable tokamak operating space through rotational stabilization of the resistive wall mode.

(2) Using rotational stabilization of the RWM, we have achieved $\beta_N H_{89} > 10$ for 4 τ_E limited by the neoclassical tearing mode.

(3) Using real-time feedback of the ECCD location, we have stabilized the (3,2) neoclassical tearing mode and then increased β_T by 60%.

(4) We have produced ECCD stabilization of the (2,1) neoclassical tearing mode in initial experiments.

(5) We have made the first integrated AT demonstration discharges with current profile control using ECCD.

(6) ECCD and ECH have been used to control the pressure profile in high performance plasmas.

(7) We have demonstrated stationary tokamak operation for 6.5 s (36 τ_E) at the same fusion gain parameter of $\beta_N H_{89}/q_{95}^2 \cong 0.4$ as ITER but at much higher $q_{95} = 4.2$.

We have developed general improvements applicable to conventional and advanced tokamak operating modes:

(1) We have an existence proof of a mode of tokamak operation, quiescent H-mode, which has no pulsed, ELM heat load to the divertor and which can run for long periods of time (3.8 s or 25 τ_E) with constant density and constant radiated power.

(2) We have demonstrated real-time disruption detection and mitigation for vertical disruption events using high pressure gas jet injection of noble gasses.

(3) We have found that the heat and particle fluxes to the inner strike points of balanced, double-null divertors are much smaller than to the outer strike points..

We have made detailed investigations of the edge pedestal and SOL:

(1) Atomic physics and plasma physics both play significant roles in setting the width of the edge density barrier in H-mode.

(2) Conducted ELM heat flux to the divertor decreases as density increases.

(3) Intermittent, bursty transport contributes to cross field particle transport in the SOL of H-mode and, especially, L-mode plasmas.

REFERENCES

[1] T.S. Taylor, H.E. St. John, A.D. Turnbull, Y.R. Lin-Liu, K.H. Burrell, V.S. Chan, M.S. Chu, J.R. Ferron, L.L. Lao, R.J. La Haye, E.A. Lazarus, R.L. Miller, P.A. Politzer, D.P. Schissel, E.J. Strait, Plasma Physics and Controlled Fusion Research **36**, B229 (1994).

[2] J. Manickam, M.S. Chance, S.C. Jardin, C. Kessel, D. Monticello, N. Pomphrey, A. Reiman, C. Wang, and L.E. Zakharov, Phys. Plasmas **1**, 1601 (1994).

[3] A.D. Turnbull, T.S. Taylor, Y.R. Lin-Liu, and H.E. St.John, Phys. Rev. Lett. **74**, 718 (1995).

[4] T.S. Taylor, Plasma Physics and Controlled Fusion **39**, B47 (1997).

[5] F. Najmabadi, S.C. Jardin, M.S. Tillack, L. Waganer, and the ARIES Team, Fusion Energy 2000 (Proc. 18th Int. Conf., Sorrento. 2000), (IAEA, Vienna, 2001) CD-ROM, File FTP 2/15 and http://www.iaea.org.programmes/ripc/physics/fec2000/html/node1.htm.

[6] F. Najmabadi and the ARIES Team, Fusion Engineering and Design **38**, 3 (1997).

[7] A.M. Garofalo, T.H. Jensen, L.C. Johnson, R.J. La Haye, G.A. Navratil, M. Okabayashi, J.T. Scoville, E.J. Strait, D.R. Baker, J. Bialek, M.S. Chu, J.R. Ferron, J. Jayakumar, L.L. Lao, M.A. Makowski, H. Reimerdes, T.S. Taylor, A.D. Turnbull, M.R. Wade, and S.K. Wong, Phys. Plasmas **9**, 1997 (2002).

[8] M. Okabayashi, J. Bialek, M.S. Chance, M.S. Chu, E.D. Fredrickson, A.M. Garofalo, R. Hatcher, T.H. Jensen, L.C. Johnson, R.J. La Haye, G.A. Navratil, H. Reimerdes, J.T. Scoville, E.J. Strait, A.D. Turnbull, M.L. Walker, and the DIII-D Team, "Stabilization of the Resistive Wall Mode in DIII-D by Plasma Rotation and Magnetic Feedback," Plasma Physics and Controlled Fusion **44**, B 339 (2002).

[9] E.J. Strait, J. Bialek, M.S. Chance, M.S. Chu, A.M. Garofalo, G.L. Jackson, L.C. Johnson, R.J. La Haye, G.A. Navratil, M. Okabayashi, H. Reimerdes, J.T. Scoville, A.D. Turnbull, M.L. Walker, and the DIII-D Team, "Resistive Wall Stabilization of High Beta Plasmas in DIII–D," this conference, file EX/S2-1.

[10] M.R. Wade, T.C. Luce, J.R. Ferron, P.A. Politzer, D.P. Brennan, T.A. Casper, A.M. Garofalo, C.M. Greenfield, A.W. Hyatt, R.J Jayakumar, J.E. Kinsey, R.J. La Haye, L.L. Lao, E.A. Lazarus, J. Lohr, M.A. Makowksi, M. Murakami, M. Okabayashi, C.C. Petty, R. Prater, E.J. Strait, A.D. Turnbull, J.G. Watkins, and W.P. West, in Proc. 29th Euro. Conf. on Controlled Fusion and Plasma Physics, Madeira, Portugal, 2001 (European Physical Society, 2001), p. 1365.

[11] ITER Physics Basis Document, Nucl. Fusion **39**, 2137 (1999).

[12] R. J. La Haye, S. Guenter, D.A. Humphreys, J. Lohr, T.C. Luce, M.E. Maraschek, C.C. Petty, R. Prater, J.T. Scoville, and E.J. Strait, Phys. Plasmas **9**, 2051 (2002).

[13] T.C. Luce, R.J. La Haye, D.A. Humphries, C.C. Petty, R. Prater, M.E. Austin, D.P. Brennan, I.A. Gorelov, J.M. Lohr, F.W. Perkins, P.A. Politzer, and M.R. Wade, in Proc. 29th Euro. Conf. on Plasma Physics and Controlled Fusion, Montreaux, Switzerland, ECA Vol. 26B (European Physical Society, 2002) P-1.059.

[14] R.J. La Haye, D.A. Humphreys, J. Lohr, T.C. Luce, F.W. Perkins, C.C. Petty R. Prater and E.J. Strait, "Increased Stable Beta in DIII–D by Suppression of a Neoclassical Tearing Mode Using Electron Cyclotron Current Drive and Active Feedback," this conference, file EX/S1-3.

[15] M.R. Wade, M. Murakami, T.A. Casper, J.R. Ferron, A.M. Garofalo, C.M. Greenfield, A.W. Hyatt, R.J. Jayakumar, J.E. Kinsey, L.L. Lao, J. Lohr, T.C. Luce, M.A. Makowski, C.C. Petty, P.A. Politzer, R. Prater and W.P. West, "Achieving and Sustaining Steady-State Advanced Tokamak Conditions On DIII–D," this conference file EX/P3-13.

[16] E.J. Doyle, T.A. Casper, K.H. Burrell, C.M. Greenfield, W.P. West, R.V. Budny, J.C. DeBoo, A.M. Garofalo, P. Gohil, R.J. Groebner, A.W. Hyatt, G.L. Jackson, T.C. Jernigan, J.E. Kinsey, L.L. Lao, C.J. Lasnier, J.-N. Leboeuf, T.C. Luce, M.A. Makowski, G.R. McKee, R.A. Moyer, M. Murakami, T.H. Osborne, W.A. Peebles, C.C. Petty, M. Porkolab, G.D. Porter, T.L. Rhodes, J.C. Rost, D.L. Rudakov, G.M. Staebler, E.J. Strait, M.R. Wade, G. Wang, J.G. Watkins, and L. Zeng, "Core and Edge Aspects of Quiescent Double Barrier Operation on DIII-D, With Relevance to Critical ITB Physics Issues," this conference file EX/C3-2.

[17] W.P. West, M.R. Wade, C.M. Greenfield, E.J. Doyle, K.H. Burrell, N.H. Brooks, P. Gohil, R.J. Groebner, G.L. Jackson, J.E. Kinsey, C.J. Lasnier, J. Mandrekas, G.R. McKee, T.L. Rhodes, G.M. Staebler, G. Wang, J.G. Watkins, and L. Zeng, Phys. Plasmas **9**, 1970 (2002).

[18] M.R. Wade, T.C. Luce, P.A. Politzer, J.R. Ferron, A.W. Hyatt, J.T. Scoville, R.J. La Haye, J.E. Kinsey, C.J. Lasnier, M. Murakami, C.C. Petty, in Proc. 29th Euro. Conf. on Plasma Physics and Controlled Fusion, Montreaux, Switzerland, ECA Vol. 26B, (European Physical Society, 2002) O-2.08 .

[19] K.H. Burrell, M.E. Austin, D.P. Brennan, J.C. DeBoo, E.J. Doyle, C. Fenzi, C. Fuchs, P. Gohil, C.M. Greenfield, R.J. Groebner, L.L. Lao, T.C. Luce, M.A. Makowski, G.R. McKee, R.A. Moyer, C.C. Petty, M. Porkolab, C.L. Rettig, T.L. Rhodes, J.C. Rost, B.W. Stallard, E.J. Strait, E.J. Synakowski, M.R. Wade, J.G. Watkins, and W.P. West Phys. Plasmas **8**, 2153 (2001).

[20] K.H. Burrell, M.E. Austin, D.P. Brennan, J.C. DeBoo, E.J. Doyle, P. Gohil, C.M. Greenfield, R.J. Groebner, L.L. Lao, T.C. Luce, M.A. Makowski, G.R. McKee, R.A. Moyer, T.H. Osborne, M. Porkolab, T.L. Rhodes, J.C. Rost, M.J. Schaffer, B.W. Stallard, E.J. Strait, M.R. Wade, G. Wang, J.G. Watkins, W.P. West, and L. Zeng, Plasma Phys. Control. Fusion **44**, A253 (2002).

[21] D.G. Whyte, T.C. Jernigan, D.A. Humphreys, A.W. Hyatt, C.J. Lasnier, P.B. Parks, T.E. Evans, M.N. Rosenbluth, P.L. Taylor, A.G. Kellman, D.S. Gray, E.M. Hollmann, and S.K. Combs, Phys. Rev. Lett. **89**, 055001 (2002).

[22] D.G. Whyte, T.C. Jernigan, D.A. Humphreys, A.W. Hyatt, C.J. Lasnier, P.B. Parks, T.E. Evans, P.L. Taylor, A.G. Kellman, D.S. Gray, E.M. Hollmann, "Disruption Mitigation With High-Pressure Noble Gas Injection," J. Nucl. Mater. (to be published).

[23] D.G. Whyte, T.C. Jernigan, D.A. Humphreys, A.W. Hyatt, C.J. Lasnier, P.B. Parks, T.E. Evans, P.L. Taylor, A.G. Kellman, D.S. Gray, E.M. Hollmann, S.C. Luckhardt, "Disruption Mitigation Using High-Pressure Noble Gas Injection on DIII–D," this conference file EX/S2-4.

[24] T.W. Petrie, C.M. Greenfield, R.J. Groebner, A.W. Hyatt, R.J. La Haye, *et al.*, J. Nucl. Mater. **290–293**, 935 (2001).

[25] T.W. Petrie, J.G. Watkins, L.R. Baylor, N.H. Brooks, M.E. Fenstermacher, *et al.*, "Changes in Edge and Scrape-Off Layer Behavior Due to Variation in Magnetic Balance in DIII–D," to be published in J. Nucl. Mater. (2002).

[26] R.J. Groebner, M.A. Mahdavi, A.W. Leonard, T.H. Osborne, G.D. Porter, Plasma Phys. and Control. Fusion **44**, A265 (2002).

[27] R.J. Groebner, M.A. Mahdavi, A.W. Leonard, T.H. Osborne, G.D. Porter, R.J. Colchin, and L.W. Owen, Phys. Plasmas **9**, 2134 (2002).

[28] M.A. Mahdavi, R.J. Groebner, A.W. Leonard, T.C. Luce, G.R. McKee, R.A. Moyer, T.H. Osborne, G.D. Porter, G. Wang and D.G. Whyte, in Proc. 20th Euro. Conf. on Plasma Physics and Controlled Fusion, Montreaux, Switzerland, ECA Vol. 26B, (European Physical Society, 2002) P-2.098.

[29] R.J. Groebner, M.A. Mahdavi, R.L. Boivin, A.W. Leonard, T.H. Osborne, G.D. Porter, N.S. Wolf, R.J. Colchin, L.W. Owen, "Correlation of H–Mode Barrier Width and Neutral Penetration Length," this conference file EX/C2-3.

[30] A.W. Leonard, J.A. Boedo, M.E. Fenstermacher, R.J. Groebner, M. Groth, C.J. Lasnier, M.A. Mahdavi, T.H. Osborne, D.L. Rudakov, T.W. Petrie, J.G. Watkins, "Transport of ELM Energy and Particles Into the SOL and Divertor of DIII-D," J. Nucl. Mater. (to be published).

[31] J.A. Boedo, D.L. Rudakov, R.A. Moyer, S. Krasheninnikov, W.P. West, S.L. Allen, T.E. Evans, R. Fonck, E. Hollman, A.W. Leonard, M.A. Mahdavi, G.D. Porter, M. Tillack, and G. Antar, Phys. Plasmas **8**, 4826 (2001).

[32] J.A. Boedo, D.L. Rudakov, R.J. Colchin, R.A. Moyer, S. Krasheninnikov, D.G. Whyte, G.R. McKee, M.J. Schaffer, P.C. Stangeby, W.P. West, S.L. Allen, A.W. Leonard, "Intermittent Convection in the Boundary of DIII-D," J. Nucl. Mater. (to be published).

[33] D.L. Rudakov, J.A. Boedo, R.A. Moyer, S. Krasheninnikov, A.W. Leonard, M.A. Mahdavi, G.R. McKee, G.D. Porter, P.C. Stangeby, J.G. Watkins, W.P. West, D.G. Whyte, and G. Antar, Plasma Phys. Control. Fusion **44**, 717 (2002).

[34] A. Bondeson and D. Ward, Phys. Rev. Lett. **72**, 2709 (1994).

[35] D.J. Ward and A. Bondeson, Phys. Plasmas **2**, 1570 (1995).

[36] A.M. Garofalo, A.D. Turnbull, M.E. Austin, J. Bialek, M.S. Chu, K.J. Comer, E.D. Fredrickson, R.J. Groebner, R.J. La Haye, L.L. Lao, E.A. Lazarus, G.A. Navratil, T.H. Osborne, B.W. Rice, S.A. Sabbagh, J.T. Scoville, E.J. Strait, and T.S. Taylor, Phys. Rev. Lett. **82**, 3811 (1999).

[37] A. Boozer, Phys. Rev. Lett. 86, 1176 (2001).

[38] M. Okabayashi, J. Bialek, M.S. Chance, M.S. Chu, E.D. Fredrickson, A.M. Garofalo, R. Hatcher, T.H. Jensen, L.C. Johnson, R.J. La Haye, M.A. Makowski, G.A. Navratil, E.A. Lazarus, J.T. Scoville, E.J. Strait, A.D. Turnbull, M.L. Walker, and the DIII-D Team, "Resistive Wall Mode Control on the DIII-D Device," General Atomics Report GA-A23892, J. Plasma Fusion Research, Vol. 5 (2002), to be published.

[39] A.M. Garofalo, R.J. La Haye and J.T. Scoville, "Analysis and Correction of Intrinsic Non-Axisymmetric Magnetic Fields in High Beta DIII-D Plasmas," Nucl. Fusion **42**, 1335 (2002).

[40] D.Gregoratto, A. Bondeson, M.S. Chu, and A.M. Garofalo, Plasma Phys. and Control. Fusion **43**, 1425 (2001).

[41] L.C. Johnson, M. Okabayashi, A.M. Garofalo, E.J. Strait, J. Bialek, M.S. Chance, M.S. Chu, E.D. Fredrickson, R.J. La Haye, J. Manickam, A. Nagy, G.A. Navratil, R.T. Snider, J.T. Scoville, A.D. Turnbull, and M.L. Walker, in Proc. 28th Euro. Conf. on Controlled Fusion and Plasma Physics, Funchal, 2001 (European Physical Society, 2001) Conference Abstracts 25A, 1361 (2001).

[42] J. Bialek, A.H. Boozer, M.E. Mauel, and G.A. Navratil, Phys. Plasmas **8**, 2170 (2001).

[43] M. Okabayashi, J. Bialek, M.S. Chance, M.S. Chu, E.D. Fredrickson, A.M. Garofalo, M. Gryaznevich, R.E. Hatcher, T.H. Jensen, L.C. Johnson, R.J. La Haye, E.A. Lazarus, M.A. Makowski, J. Manickam, G.A. Navratil, J.T. Scoville, E.J. Strait, A.D. Turnbull, M.L. Walker, DIII-D Team, Phys. Plasmas **8**, 2071 (2001).

[44] Y.Q. Lin, A. Bondeson, C.M. Fransson, B. Lennartson, and C. Breitholtz, Phys. Plasmas **7**, 3681 (2000).

[45] M.S. Chu, M.S. Chance, A.H. Glasser, M. Okabayashi, V.S. Chan, S.C. Guo, D.A. Humphreys, T.H. Jensen, L.L. Lao, F.W. Perkins, H.E. St.John, E. Soon, A.D. Turnbull, M.L. Walker, and S.K. Wong, "Modeling of Feedback and Rotation Stabilization of the Resistive Wall Mode in Tokamaks," this conference, file TH/P3–10.

[46] O. Sauter, R.J. La Haye, Z. Chang, D.A. Gates, Y. Kamada, H. Zohm, A. Bondeson, D. Boucher, J.D. Callen, M.S. Chu, T.A. Gianakon, O. Grueber, R.W. Harvey, C.C. Hegna, L.L. Lao, D.A. Monticello, F.W. Perkins, A. Pletzer, A.H. Reiman, M.N. Rosenbluth, E.J. Strait, T.S. Taylor, A.D. Turnbull, F. Waelbroeck, J.C. Wesley, H.R. Wilson, and R. Yoshino, Phys. Plasmas **4**, 1654 (1997).

[47] C.C. Hegna and J.D. Callen, Phys. Plasmas **4**, 2940 (1997).

[48] H. Zohm, Phys. Plasmas **4**, 3433 (1997).

[49] G. Gantenbein, H. Zohm, G. Giruzzi, S. Guenter, F. Leuterer, M. Maraschek, J. Meskat, Q. Yu, ASDEX Upgrade Team, and ECRH-Group (AUG), Phys. Rev. Lett. **85**, 1242 (2000).

[50] S.L. Allen, DIII-D Team, Nucl. Fusion **41**, 1341 (2001).

[51] C.C. Petty, R. Prater, J. Lohr, T.C. Luce, W.R. Fox, R.W. Harvey, J.E. Kinsey, L.L. Lao, and M.A. Makowski, Nucl. Fusion **42**. 1366 (2002).

[52] C.C. Petty, R. Prater, T.C. Luce, R.A. Ellis, R.W. Harvey, J.E. Kinsey, L.L. Lao, J. Lohr, M.A. Makowski, and K.-L. Wong, "Physics of Electron Cyclotron Current Drive on DIII-D," this conference file EX/W-4.

[53] R.W. Harvey, M.G. McCoy, Proc. of the IAEA Technical Committee Meeting, Montreal, Canada, 1992 (International Atomic Energy Agency, Vienna, 1993) 498.

[54] B.W. Rice, D.G. Nilson, K.H. Burrell, and L.L. Lao, Rev. Sci. Instrum. **70**, 815 (1999).

[55] A.D. Turnbull, T.S. Taylor, and M.S. Chu, Nucl. Fusion **38**, 1467 (1998).

[56] V.V. Alikaev, et al., Fiz. Plasmy **2**, 390 (1976) [Sov. J. Plasma Phys. **2**, 212 (1976)].

[57] M. Kotschenreuther, G. Rewoldt and W.M. Tang, Comp. Phys. Comm. **88**, 128 (1995).

[58] C.C. Petty, T.C. Luce, D.R. Baker, B. Balet, T.N. Carlstrom, J.G. Cordey, J.C. DeBoo, P. Gohil, R.J. Groebner, B.W. Rice, D.M. Thomas, M.R. Wade, and R.E. Waltz, Phys. Plasmas **5**, 1695 (1998).

[59] R.E. Waltz, G.M. Staebler, W. Dorland, G.W. Hammett, M. Kotschenreuther, and J.A. Konings, Phys. Plasmas **4**, 2482 (1997).

[60] J.E. Kinsey, T. Onjun, G. Bateman, A. Kritz, A. Pankin, G.M. Staebler, and R.E. Waltz, "Burning Plasma Projections Using Drift Wave Transport Models and Scaling For the H-Mode Pedestal," this conference file TH/P1-09

[61] J.E. Kinsey, G.M. Staebler, R.E. Waltz, Phys. Plasmas **9**, 1676 (2002).

[62] M. Greenwald, J.L. Terry, S.M. Wolfe, S. Ejima, M.G. Bell, S.M. Kaye, G.H. Neilson, Nucl. Fusion **28**, 2199 (1988).

[63] T.W. Petrie, L.L. Lao, P.B. Snyder, and J.G. Watkins, "The Role of Magnetic Balance on the Poloidal Distribution of ELM-Induced Peak Particle Flux at the Divertor Targets in DIII-D," submitted to Nucl. Fusion.

[64] W. Suttrop, M. Kaufmann, H.J. de Blank, et al., Plasma Phys. Control. Fusion **39**, 2051 (1997).

[65] T.H. Osborne, J.R. Ferron, R.J. Groebner, L.L. Lao, A.W. Leonard, R. Maingi, R.L. Miller, A.D. Turnbull, M.R. Wade, Plasma Phys. Control. Fusion **40**, 845 (1998).

[66] M. Greenwald, R.L. Boivin, F. Bombarda, *et al.*, Nucl. Fusion 37, 793 (1997).

[67] P.B. Snyder, H.R. Wilson, J.R. Ferron, *et al.*, Phys. Plasmas **9**, 2037 (2002).

[68] P.B. Snyder, H.R. Wilson, X.Q. Xu, J.R. Ferron, L.L. Lao, A.W. Leonard, D. Mossessian, M. Murakami, T.H. Osborne, A.D. Turnbull, "ELMs and Constraints on the H-Mode Pedestal: A Model Based on Peeling-Ballooning Modes," this conference file TH/3-1..

[69] T.D. Rognlien, M.E. Rensink, Fusion Eng. and Design **60**, 497 (2002).

[70] A.W. Leonard, A. Herrmann, K. Itami, *et al.*, J. Nucl. Mater **266-269**, 109 (1999).

[71] G. Janeschitz, *et al..,* J. Nucl. Mater. **290-293**, 1 (2000).
[72] A.W. Leonard, R.J. Groebner, M.A. Mahdavi, *et al.,* Plasma Phys. Control. Fusion **44**, 945 (2002).
[73] J. Stober, M. Maraschek, G.D. Conway, *et al.*, Nucl. Fusion **41**, 1123 (2001).
[74] D. D'Ippolito, J. Myra, S. Krasheninnikov, Phys. Plasmas **9**, 222 (2002).
[75] S. Krasheninnikov, Phys. Lett. A **283**, 268 (2001).
[76] X.Q. Xu, Lawrence Livermore National Laboratory private communication (2002).

ACKNOWLEDGMENT

This work was supported in part by the U.S. Department of Energy under Contract No. DE-AC03-99ER54463.